



Raining in MKW 3 s: A Chandra-MUSE Analysis of X-Ray Cold Filaments around 3CR 318.1

A. Jimenez-Gallardo^{1,2,3,4}, F. Massaro^{1,3,4,5}, B. Balmaverde⁴, A. Paggi^{1,3,4}, A. Capetti⁴, W. R. Forman⁶, R. P. Kraft⁶, R. D. Baldi^{7,8}, V. H. Mahatma⁹, C. Mazzucchelli², V. Missaglia^{1,3,4}, F. Ricci^{10,11}, G. Venturi^{12,13}, S. A. Baum¹⁴, E. Liuzzo⁷, C. P. O'Dea¹⁴, M. A. Prieto^{15,16}, H. J. A. Röttgering¹⁷, E. Sani², W. B. Sparks^{18,19}, G. R. Tremblay⁶, R. J. van Weeren¹⁷, B. J. Wilkes⁶, J. J. Harwood²⁰, P. Mazzotta²¹, and J. Kuraszkiewicz⁶

¹ Dipartimento di Fisica, Università degli Studi di Torino, via Pietro Giuria 1, I-10125 Torino, Italy; ana.jimenezgallardo@edu.unito.it

² European Southern Observatory, Alonso de Córdova 3107, Vitacura, Región Metropolitana, Chile

³ Istituto Nazionale di Fisica Nucleare, Sezione di Torino, I-10125 Torino, Italy

⁴ INAF-Osservatorio Astrofisico di Torino, via Osservatorio 20, I-10025 Pino Torinese, Italy

⁵ Consorzio Interuniversitario per la Fisica Spaziale, via Pietro Giuria 1, I-10125 Torino, Italy

⁶ Center for Astrophysics | Harvard & Smithsonian, 60 Garden Street, Cambridge, MA 02138, USA

⁷ Istituto di Radioastronomia, INAF, via Gobetti 101, I-40129, Bologna, Italy

⁸ Department of Physics & Astronomy, University of Southampton, Hampshire SO17 1BJ, Southampton, UK

⁹ Thüringer Landessternwarte, Sternwarte 5, D-07778 Tautenburg, Germany

¹⁰ Dipartimento di Fisica e Astronomia dell'Università degli Studi di Bologna, via P. Gobetti 93/2, I-40129 Bologna, Italy

¹¹ INAF- Osservatorio di Astrofisica e Scienza dello Spazio di Bologna, via Gobetti 93/3, I-40129 Bologna, Italy

¹² Instituto de Astrofísica, Facultad de Física, Pontificia Universidad Católica de Chile, Casilla 306, Santiago 22, Chile

¹³ INAF—Osservatorio Astrofisico di Arcetri, Largo E. Fermi 5, I-50125 Firenze, Italy

¹⁴ University of Manitoba, Dept. of Physics and Astronomy, Winnipeg, MB R3T 2N2, Canada

¹⁵ Departamento de Astrofísica, Universidad de La Laguna, E-38206 La Laguna, Tenerife, Spain

¹⁶ Instituto de Astrofísica de Canarias (IAC), E-38200 La Laguna, Tenerife, Spain

¹⁷ Leiden Observatory, Leiden University, PO Box 9513, 2300 RA Leiden, The Netherlands

¹⁸ SETI Institute, Mountain View, CA 94043, USA

¹⁹ Space Telescope Science Institute, 3700 San Martin Drive, Baltimore, MD 21218, USA

²⁰ Centre for Astrophysics Research, School of Physics, Astronomy and Mathematics, University of Hertfordshire, College Lane, Hatfield, Hertfordshire AL10 9AB, UK

²¹ Dipartimento di Fisica, Università di Roma “Tor Vergata,” Via della Ricerca Scientifica 1, I-00133 Rome, Italy

Received 2021 February 12; revised 2021 April 7; accepted 2021 April 12; published 2021 May 10

Abstract

We present the analysis of X-ray and optical observations of gas filaments observed in the radio source 3CR 318.1, associated with NGC 5920, the brightest cluster galaxy (BCG) of MKW 3 s, a nearby cool core galaxy cluster. This work is one of the first X-ray and optical analyses of filaments in cool core clusters carried out using MUSE observations. We aim at identifying the main excitation processes responsible for the emission arising from these filaments. We complemented the optical VLT/MUSE observations, tracing the colder gas phase, with X-ray Chandra observations of the hotter highly ionized gas phase. Using the MUSE observations, we studied the emission line intensity ratios along the filaments to constrain the physical processes driving the excitation, and, using the Chandra observations, we carried out a spectral analysis of the gas along these filaments. We found a spatial association between the X-ray and optical morphology of these filaments, which are colder and have lower metal abundance than the surrounding intracluster medium (ICM), as already seen in other BCGs. Comparing with previous results from the literature for other BCGs, we propose that the excitation process that is most likely responsible for these filaments emission is a combination of star formation and shocks, with a likely contribution from self-ionizing, cooling ICM. Additionally, we conclude that the filaments most likely originated from AGN-driven outflows in the direction of the radio jet.

Unified Astronomy Thesaurus concepts: Active galactic nuclei (16); Radio active galactic nuclei (2134); Galaxy clusters (584); Cool cores (302)

1. Introduction

The Third Cambridge Catalog of radio sources and its revised versions (3C, 3CR, 3CRR; Edge et al. 1959; Bennett 1962; Spinrad et al. 1985; Laing et al. 1983) constitute one of the most valuable samples of radio-loud active galactic nuclei (AGN). In 2018, Balmaverde et al. (2018) started the MUSE Radio Loud Emission line Snapshot (MURALES) survey to observe all southern 3CR sources with the Multi-Unit Spectroscopic Explorer (MUSE; Bacon et al. 2010) and enrich the multifrequency coverage of the 3CR catalog.

During the MURALES survey, an optical filamentary structure was detected in 3CR 318.1 (Balmaverde et al.

2019), the brightest cluster galaxy (BCG) of the galaxy cluster MKW 3 s (Morgan et al. 1975), in agreement with observations by Edwards et al. (2009). This structure consists of two ionized gas filaments extending \sim 25 kpc in the south and the southwest directions, both with almost constant velocities along their projected lengths (\sim 230 km s $^{-1}$ and \sim 280 km s $^{-1}$, respectively). The filament that points to the south presents a bright knot at its southern end. In contrast with the typical narrow-line regions seen in other radio galaxies, these filaments extend beyond tens of kiloparsecs and present drastically different emission line ratios (e.g., [O III]/H $_{\beta}$ \sim 0.1 instead of the typical value of \sim 10).

Similar filamentary structures were discovered in other BCGs, as NGC 1275 in the center of the Perseus galaxy cluster (Lynds 1970; Conselice et al. 2001 and Fabian et al. 2008), spatially associated with an X-ray excess (Fabian et al. 2011). The same situation occurs for other BCGs, where a tight connection between X-ray and optical filament emission was found (McDonald et al. 2010).

However, the physical processes responsible for the ionization in these optical filaments is still debated. While Voit et al. (1994) proposed ionization due to hot cooling intracluster medium (ICM) as the excitation mechanism behind these filaments, McDonald et al. (2010), who analyzed a sample of 23 filaments around BGCs, suggested that these types of filaments are due to ICM thermal conduction. In the case of the Perseus cluster, Fabian et al. (2011) rejected this scenario, due to the lack of a thick interface between the cold and hot gas, proposing that the origin of cold X-ray filaments is due to penetration of cold gas by the hot surrounding gas through reconnection diffusion.

Here we present a comparison between optical and X-ray images of 3CR 318.1 to investigate the main ionization processes underlying the origin of these optical filaments, thus focusing only on the first ~ 30 kpc at the center of MKW 3 s (for works on the large-scale structures see, e.g., Mazzotta et al. 2002, 2004; Bîrzan et al. 2020).

This paper is organized as follows. A brief description of 3CR 318.1 is given in Section 2. Optical and X-ray data analyses are reported in Section 3. Results are presented in Section 4, while Section 5 is devoted to our conclusions.

Unless otherwise stated, we adopted cgs units for numerical results and assumed a flat cosmology with $H_0 = 69.6 \text{ km s}^{-1} \text{ Mpc}^{-1}$, $\Omega_M = 0.286$, and $\Omega_\Lambda = 0.714$ (Bennett et al. 2014). Spectral indices, α , are defined by flux density, $S_\nu \propto \nu^{-\alpha}$.

2. 3CR 318.1

3CR 318.1 is the radio source associated with the nearby ($z = 0.0453$, which corresponds to $0.896 \text{ kpc arcsec}^{-1}$) galaxy NGC 5920, the BCG of the galaxy cluster MKW 3 s. Based on its optical line emission, it can be classified as an extremely low-excitation galaxy (see Capetti et al. 2013). The central source presents a steep spectrum at low radio frequencies (i.e., $\alpha_{1.4 \text{ GHz}}^{150 \text{ MHz}} = 0.63$) with a luminosity of $\log L_{150 \text{ MHz}} = 23.16 \text{ W Hz}^{-1}$ (Capetti et al. 2020). The surrounding diffuse radio emission also shows an extremely steep radio spectrum ($\alpha_{235 \text{ MHz}}^{1.28 \text{ GHz}} = 2.42$), leading to a classification of relic radio galaxy by Giacintucci et al. (2007). The host galaxy of 3CR 318.1 presents an AB UV magnitude at 2600 \AA of 19.04 ± 0.04 , corrected for Galactic reddening (Cardelli et al. 1989), with $E(B - V) = 0.0356 \pm 0.0010$.²² This magnitude yields a UV luminosity at 2600 \AA of $L_{\text{UV}} = (4.96 \pm 0.17) \times 10^{42} \text{ erg s}^{-1}$. An overview of 3CR 318.1 and its environment is shown in Figure 1.

Peres et al. (1998) found that MKW 3 s presents a moderate “cooling flow” ($\dot{M} \sim 170 M_\odot \text{ yr}^{-1}$). Using deep (~ 57 ks) Chandra X-ray observations of the central 200 kpc, Mazzotta et al. (2002) identified the presence of a cavity, located at ~ 90 kpc south of the X-ray nucleus, hotter than the ~ 3 keV average cluster temperature and filled by radio emission arising from the southern lobe (Mazzotta et al. 2004), as recently confirmed

by Bîrzan et al. (2020) using Low Frequency Array observations.

3. Data Reduction and Analysis

X-ray data reduction was performed following standard procedures of the Chandra Interactive Analysis of Observations v4.10 (CIAO; Fruscione et al. 2006) threads²³, adopting the Chandra Calibration Database v4.8.4.1, and using the ~ 57 ks Chandra observation (ObsID 900). The MUSE data set was obtained from the MURALE survey (ID 099.B-0137(A); two exposures of 10 minutes each), with a mean seeing in the V band at zenith of $1''.38$ (see Balmaverde et al. 2019 for details on the data reduction and analysis). Here we focus on the analysis of the $[\text{N II}] \lambda 6584$ emission since it is more luminous and extended than the $\text{H}\alpha$ emission. The $[\text{N II}]/\text{H}\alpha$ ratio is constant along filaments with $[\text{N II}]/\text{H}\alpha \sim 1.9$.

Astrometric registration to align radio, optical, and X-ray images was performed by measuring the radio centroid at 1.4 GHz (beam size of $4''.5$), and the X-ray centroid in the 0.5–7 keV energy range and then aligning them following the procedure from Massaro et al. (2011a). We shifted the X-ray image $0.568''$ to the northeast; then, we aligned the position of the optical host galaxy in the MUSE continuum image with the radio centroid shifting it by $1''.62$. These shifts are consistent with those previously reported for the 3CR Chandra Snapshot Survey (Massaro et al. 2011a, 2013, 2015, 2018; Jimenez-Gallardo et al. 2020). Registration was then verified by checking the alignment of other pointlike field sources in the Sloan Digital Sky Survey (SDSS) and in the MUSE continuum images. The comparison between registered X-ray and $[\text{N II}] \lambda 6584$ optical images is shown in Figure 2.

In the same figure, we show the regions selected to perform X-ray spectral analysis, based on the morphology of the $[\text{N II}] \lambda 6584$ emission. These, labeled according to the nomenclature of Massaro et al. (2011a), are

1. two circles of $2''$ radius, centered on (i) the radio core and (ii) the $[\text{N II}] \lambda 6584$ emission line knot at the end of the south filament (core and s14, respectively);
2. two polygons along the southwest filament, namely, sw4 (inner 4 kpc) and sw14 (remaining 13 kpc).

We chose, as background for the spectral analysis of the filament regions, a larger circle located $\sim 45''$ to the northeast where no pointlike and/or extended X-ray sources are detected, to obtain the spectrum of the excess emission only instead of the line-of-sight average. We also performed the spectral analysis of the galaxy cluster emission, considering two polygonal regions, one at each side of the filaments and a background region at $\sim 100''$ to compare the inner and outer galaxy cluster emission.

Background-subtracted X-ray spectra in the 0.5–4 keV energy range were extracted using the CIAO routine SPECEXTRACT and the background region containing neighboring ICM emission to the filament and analyzed using Sherpa v4.12.1 (Freeman et al. 2001). To ensure the validity of Gaussian statistics, spectral data were binned to at least 25 photons per bin.

We tried fitting the final spectra using an absorbed bremsstrahlung model; however, it failed to reproduce the soft X-ray excess below 2 keV. Thus, we adopted a collisional

²² <https://irsa.ipac.caltech.edu/applications/DUST/>

²³ <http://cxc.harvard.edu/ciao/threads/>

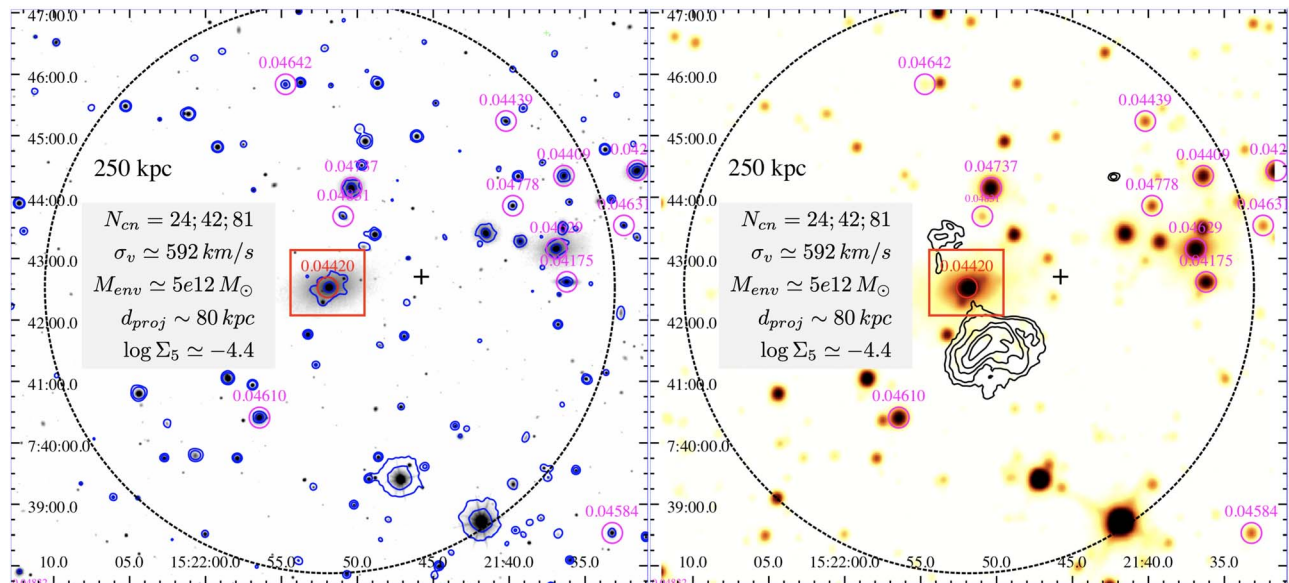


Figure 1. r -band SDSS image with SWIFT UV contours at 2600 Å overlaid in blue (left) and 3.4 μm WISE image with 328 MHz VLA radio contours overlaid in black (right), showing 3CR 318.1 at the center and other sources in the field. The red squares show MUSE field of view. Radio contours were drawn at 5, 10, 20, 40, and 80 times the rms level of the background in the radio map (beam size of 5. $''$). Sources in the field with known spectroscopic redshifts are marked in magenta. Ambient parameters, shown in both panels, were derived according to Massaro et al. (2019, 2020, 2020). N_{cn} is the number of cosmological neighbors within a radius of 500 kpc, 1 Mpc, and 2 Mpc, respectively; σ_v is the velocity dispersion of the cosmological neighbors; M_{env} is the environmental mass (i.e., galaxies, IGM and dark matter) estimated from the velocity dispersion; d_{proj} is the projected distance between the central radio galaxy and the centroid of the position of the cosmological neighbors within 2 Mpc (marked by the black cross); and Σ_5 is the cosmological parameter used to trace the dark matter halo density (see Sabater et al. 2013; Worrel et al. 2013). SWIFT-UVOT data were reduced according to the standard procedure (see Massaro et al. 2008a, 2008b for more details).

ionization gas model (XSAPC²⁴), absorbed by Galactic hydrogen column density (XSWABS²⁵; $N_{\text{H,Gal}} = 3.8 \times 10^{20} \text{ cm}^{-2}$; Kalberla et al. 2005). The XSAPC model had three free parameters: normalization, plasma temperature kT , and metal abundance Z .

We confirmed the presence of a soft X-ray (i.e., 0.5–3 keV) excess spatially coincident with the [N II] $\lambda 6584$ filament (regions sw4 and sw14) at a level of confidence $>5\sigma$ with respect to the surrounding ICM emission. Detection significance, reported in Gaussian equivalent, was computed assuming a Poisson distribution of photons in the inner background region.

Assuming the presence of emission lines below 2 keV (see Section 4), we created narrowband X-ray images, shown in Figure 3 (see, e.g., Massaro et al. 2013, 2015, 2018). We chose three energy ranges mainly attributable to (i) Fe (0.9–1.2 keV), (ii) Mg (1.2–1.5 keV), and (iii) S+Si (1.6–2.1 keV) ionized elements. X-ray flux maps were created by using monochromatic exposure maps set to the nominal energies of 1, 1.3, and 1.8 keV for Fe, Mg, and S+Si, respectively, to take into account the detector effective area at different energies.

From the optical perspective, we modeled the main emission lines present in the MUSE spectra, i.e., H β , H α , [O III] $\lambda 5007$, [O I] $\lambda 6300$, [N II] $\lambda 6584$, and the [S II] doublet at $\lambda\lambda 6716, 6731$ using Gaussian functions at different locations across the filament and the knot. The top panel of Figure 4 shows the MUSE spectrum of the optical knot sw14, as an example. The H β line was modeled using an additional broad component only present in the core and in region s4.

4. Results

4.1. Optical

We computed the emission line intensity ratios for all regions (see Figure 2) and plotted them in the diagnostic diagrams defined by the intensity ratios shown in Figure 4, used to distinguish between different ionization mechanisms occurring in H II regions, AGN, or LINER/shocks (Baldwin et al. 1981; Dopita & Sutherland 1995). Measurements obtained for all four regions in 3CR 318.1 are closely clustered and located where no emission line galaxies are found (see, e.g., Kewley et al. 2006; Capetti & Baldi 2011).

Similarly to what was found for filaments in different BCGs by McDonald et al. (2012), line ratios provide a contradictory classification: at the boundary between LINER and H II from the [O III]/H β versus [N II]/H α and [O I]/H α diagrams and in the region of ionization due to star formation from the [S II]/H α ratio.

We also estimated the gas density along the filaments, using the ratio of the [S II] $\lambda 6716$ and the [S II] $\lambda 6731$ lines (see Osterbrock 1989). Assuming a typical temperature of 10^4 K, we obtained $n_e \sim 1380 \text{ cm}^{-3}$ in the core and $n_e < 100 \text{ cm}^{-3}$ in s14 and along the filament (sw4 and sw14). We estimated the total mass of the ionized gas as $M = 7.5 \times 10^{-3} \left(\frac{10^4 L_{\text{H}\beta}}{n_e} \right) M_\odot$, where $L_{\text{H}\beta}$ is the H β luminosity (see Osterbrock 1989). Thus, we estimated a total ionized gas mass of $M \sim 2 \times 10^5 M_\odot$ in the core, $M > 4 \times 10^5 M_\odot$ in s14, and $M > 10^6 M_\odot$ along the filament.

Simulations carried out by Qiu et al. (2019, 2020) show that cold filaments in cool core clusters can originate from warm AGN-driven outflows with shorter cooling than rising times. These simulations are consistent with the filaments in 3CR 318.1 extending in the direction of the southern radio lobe.

²⁴ <https://cxc.cfa.harvard.edu/sherpa/ahelp/xsape.html>

²⁵ <https://cxc.cfa.harvard.edu/sherpa/ahelp/xswabs.html>

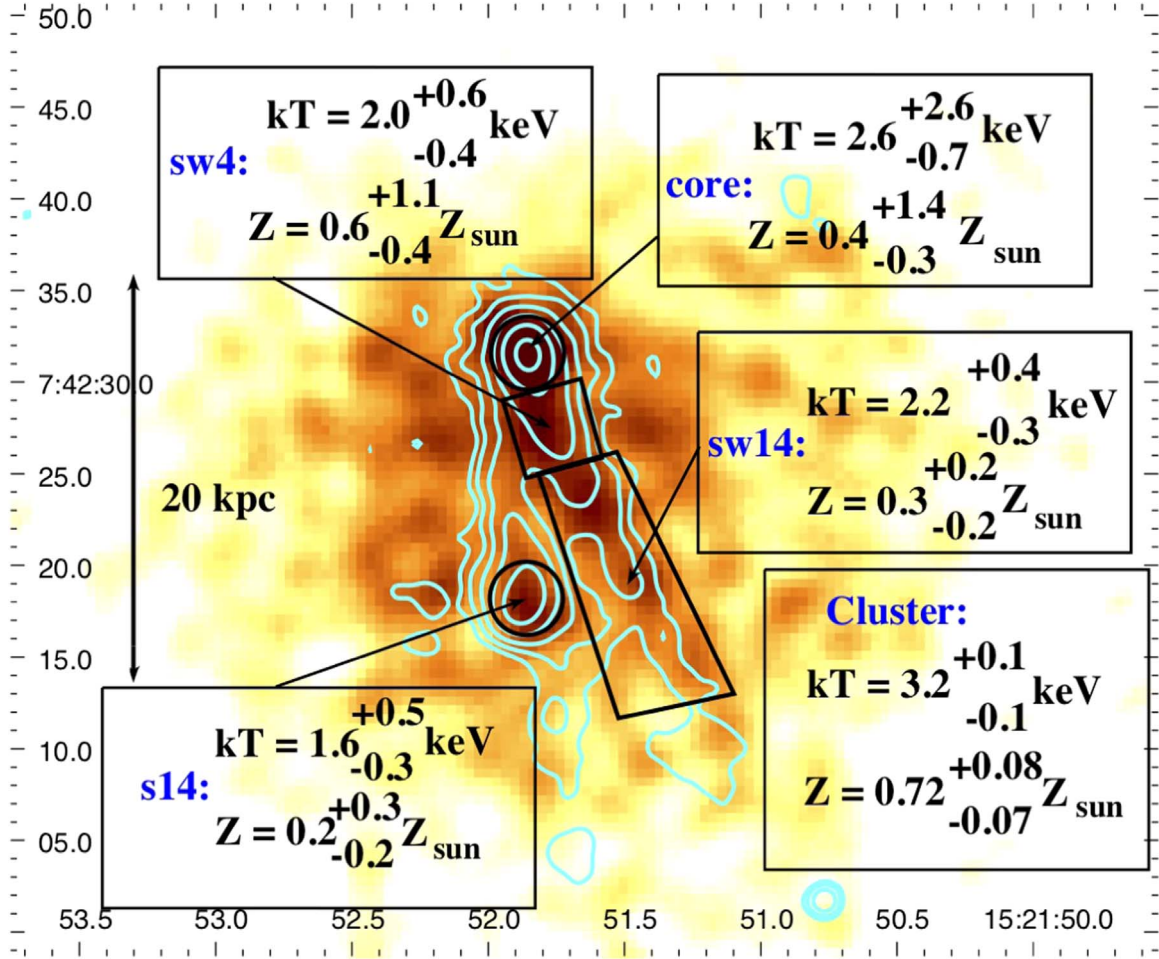


Figure 2. 0.5–3 keV Chandra image with [N II] λ 6584 emission line contours overlaid in cyan. The Chandra image was smoothed with a 2'' Gaussian kernel. [N II] λ 6584 contours were drawn at 1, 2, 4, 8, 16, and 32×10^{-20} erg s $^{-1}$ cm $^{-2}$ (starting at 3 times the rms). Regions chosen for the X-ray spectral analysis (described in Section 3) and the results for each region are shown in black. The fit for each region yielded the following reduced $\chi^2_{\nu} = 1.304$ ($\nu = 8$), with 237 net photons, for the core, $\chi^2_{\nu} = 0.900$ ($\nu = 5$), with 167 net photons, for region s14, $\chi^2_{\nu} = 0.996$ ($\nu = 10$), with 268 net photons, for region sw4, $\chi^2_{\nu} = 0.588$ ($\nu = 36$), with 845 net photons, for region sw14, and $\chi^2_{\nu} = 0.906$ ($\nu = 207$) for the cluster region.

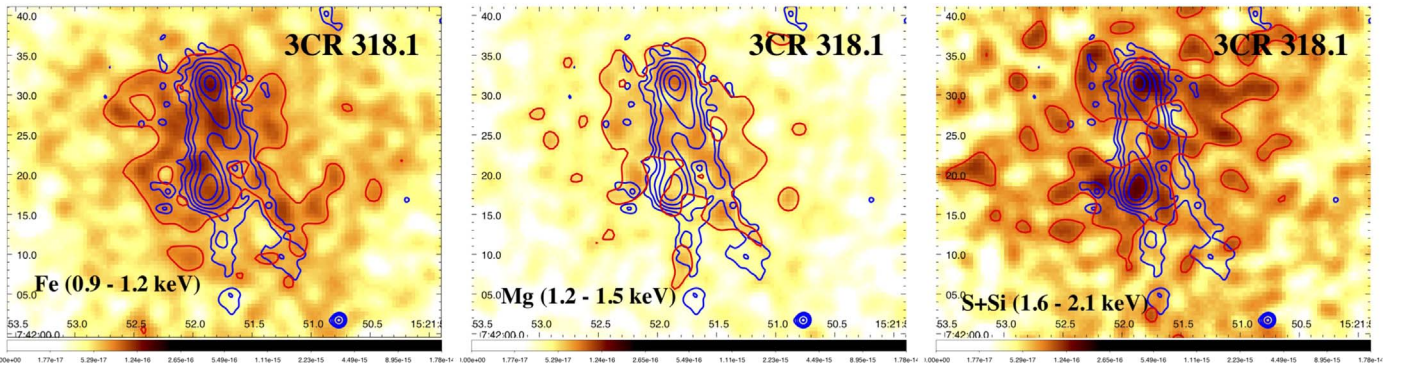


Figure 3. Narrowband Chandra flux images in the 0.9–1.2 keV (left), 1.2–1.5 keV (center), and 1.6–2.1 keV (right) energy bands to show Fe, Mg, and S+Si X-ray emissions with [N II] λ 6584 contours overlaid. Chandra images were smoothed with a Gaussian kernel of 2''. [N II] λ 6584 emission line contours are the same as in Figure 2. X-ray emission due to Mg seems to trace the [N II] λ 6584 morphology the best. X-ray fluxes along the filament (regions sw4 and sw14) are $F_{\text{Fe}} = 2.9^{+0.2}_{-0.3} \times 10^{-14}$ erg s $^{-1}$ cm $^{-2}$ in the Fe band, $F_{\text{Mg}} = 1.9^{+0.1}_{-0.1} \times 10^{-14}$ erg s $^{-1}$ cm $^{-2}$ in the Mg band, and $F_{\text{S+Si}} = 2.3^{+0.1}_{-0.2} \times 10^{-14}$ erg s $^{-1}$ cm $^{-2}$ in the S + Si band.

4.2. X-Rays

We performed the X-ray spectral analysis in all regions described in Section 3, along optical filaments and in the galaxy cluster (excluding filaments, core, and knots). Best-fit results, obtained with the absorbed XSAPEC model, are reported in

Figure 2. We also fitted regions sw4 and sw14 together and obtained a gas temperature of $2.4^{+0.3}_{-0.3}$ keV (with $Z = 0.5^{+0.3}_{-0.2} Z_{\odot}$ and reduced $\chi^2_{\nu} = 0.857$ with $\nu = 59$ degrees of freedom) for the southwestern filament. This is colder than the surrounding ICM, which has $kT = 3.2^{+0.1}_{-0.1}$ keV (reduced

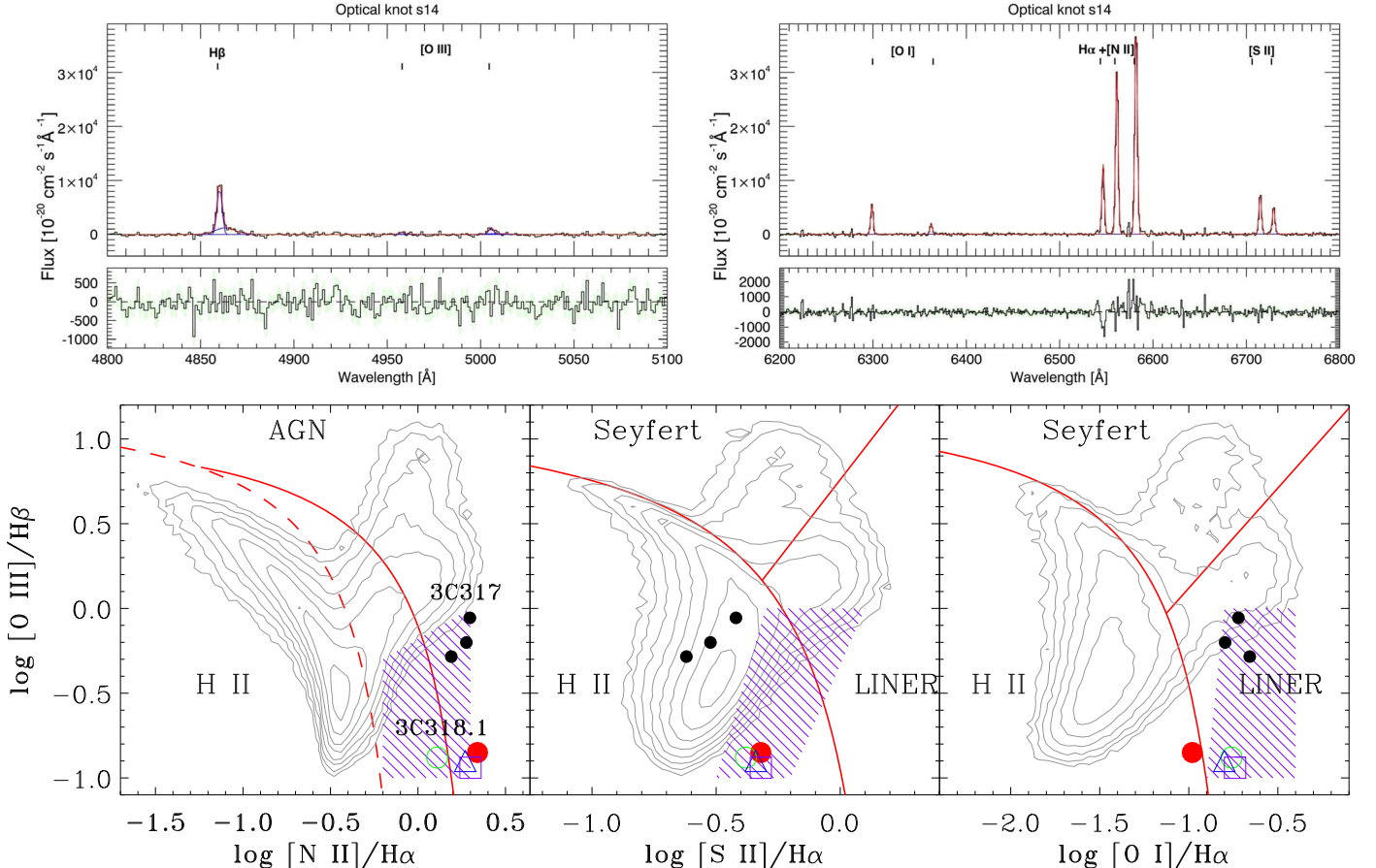


Figure 4. Top: MUSE spectrum (black histograms) of region s14; see Figure 2, in rest frame, shown as an example. We show in red the Gaussian fit of the emission lines (top panels) and the residuals (bottom panels). Bottom: location of 3CR 318.1 regions “core,” s14, sw4, and sw14 (red filled circle, green circle, blue triangle, and magenta square, respectively) in the Baldwin, Phillips & Telervich (BPT) diagnostic diagrams. The red solid curves represent the Kewley et al. (2001) theoretical upper bound for pure star formation, the red straight line shows the Kewley et al. (2006) separation between AGN and LINERs, while the dashed red curve in the [N II] $\lambda 6584$ BPT is the Kauffmann et al. (2003) empirical classification separating star-forming galaxies and AGN. Contours represent the isodensities of all SDSS/DR7 emission line galaxies (Capetti & Baldi 2011). The three black dots mark the location of the filaments in 3CR 317, the central galaxy of A2052, also observed as part of the MURALE survey (see Balmaverde et al. 2018). Purple dashed regions mark the location of filaments in other cool core galaxy clusters as measured by McDonald et al. (2012).

$\chi^2_{\nu} = 0.906$; $\nu = 207$). The ICM temperature is consistent with the average temperature found by Mazzotta et al. (2002) for the inner regions of MKW 3 s.

Metal abundance of the optical filament, $Z = 0.3^{+0.2}_{-0.2}$ for sw14 (with reduced $\chi^2_{\nu} = 0.588$; $\nu = 36$), appears to be marginally lower than that of the surrounding ICM ($Z = 0.72^{+0.08}_{-0.07}$). This is in agreement with literature results on other filaments (see, e.g., Fabian et al. 2011; McDonald et al. 2010).

Assuming that narrowband images trace the X-ray emission lines, the Mg emission has a better spatial association with the optical filaments, while Fe and S+Si show X-ray emission more extended than the filaments, as well as strong emission at the core and the s14 (knot) regions (see Figure 3). We computed the X-ray flux along the filament (regions sw4 and sw14) in the Fe, Mg, and S+Si band and compared them with optical and X-ray fluxes. The X-ray fluxes along the filament (regions sw4 and sw14) are $F_{\text{Fe}} = 2.9^{+0.2}_{-0.3} \times 10^{-14} \text{ erg s}^{-1} \text{ cm}^{-2}$ in the Fe band, $F_{\text{Mg}} = 1.9^{+0.1}_{-0.1} \times 10^{-14} \text{ erg s}^{-1} \text{ cm}^{-2}$ in the Mg band, $F_{\text{S+Si}} = 2.3^{+0.1}_{-0.2} \times 10^{-14} \text{ erg s}^{-1} \text{ cm}^{-2}$ in the S+Si band, and $F_{0.5-3 \text{ keV}} = 1.32^{+0.05}_{-0.08} \times 10^{-13} \text{ erg s}^{-1} \text{ cm}^{-2}$ in the soft band (0.5–3 keV). Detection significance of the excess X-ray emission along optical filaments is above 5σ confidence

level for both Mg and Fe, while it is not significant for the S+Si narrowband image, thus the S+Si emission along the filament is consistent with the ICM emission.

We also obtained $F_{\text{H}\alpha}/F_{\text{Fe}} = 2.9^{+0.4}_{-0.4} \times 10^{-2}$ and $F_{\text{H}\alpha}/F_{0.5-3 \text{ keV}} = 6.5^{+0.7}_{-0.8} \times 10^{-3}$. In contrast with the filaments of 3CR 318.1, Sanders & Fabian (2007) and Fabian et al. (2011) found that those in Perseus have soft X-ray emission of the same order as the H α emission, while the H α emission is an order of magnitude above the Fe emission, which highlights the much lower ionization state here. Additionally, we obtained $F_{[\text{O III}]}/F_{0.5-3 \text{ keV}} = 1.15^{+0.12}_{-0.14} \times 10^{-3}$, which is three orders of magnitude below the value obtained by Balmaverde et al. (2012) for the emission line regions in nine 3CR radio galaxies.

Finally, we derived the 0.5–3 keV, exposure-corrected, X-ray surface brightness profile with azimuthal bins of 10° centered on 3CR 318.1 core, excluding the inner $2''$ and extending up to ~ 30 kpc (see Jimenez-Gallardo et al. 2021 for additional details). We chose to make the bin containing the [N II] $\lambda 6584$ filament correspond to the 180° bin. The resulting X-ray surface brightness profile is shown in Figure 5. The background level is two orders of magnitude below the filament emission. The smooth increase of the surface brightness toward the [N II] $\lambda 6584$ filament supports the hypothesis

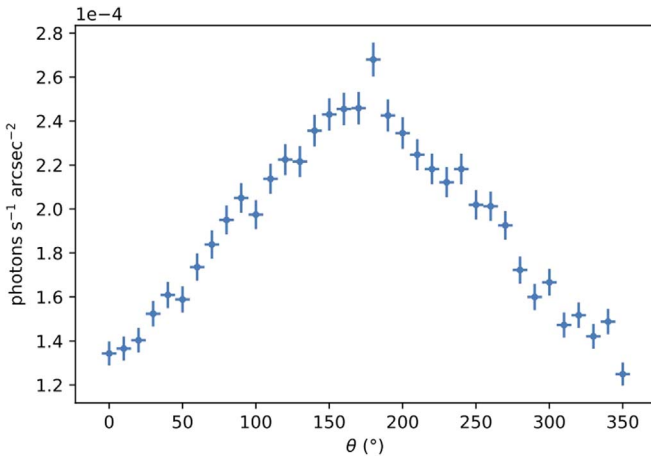


Figure 5. 0.5–3 keV, exposure-corrected, X-ray surface brightness profile with azimuthal bins of 10° centered on the core of 3CR 318.1. The bins were chosen so that the bin at 180° is the one containing the $[\text{N II}]\lambda 6584$ filament. Background level is two orders of magnitude below the filament emission. The increase of surface brightness corresponds to $[\text{N II}]\lambda 6584$.

that the filament could have originated due to outflows in the direction of the radio jets.

5. Discussion and Conclusions

The MURALE survey revealed the presence of optical filaments in 3CR 318.1, the BCG of MKW 3 s. Here we compared optical VLT/MUSE and X-ray Chandra observations to shed light on their physical origin.

From an optical perspective, intensity ratios of various rest-frame emission lines were used to distinguish between different ionization mechanisms. Possible explanations of filamentary emission include: ionization due to hot cooling ICM (Voit et al. 1994), ICM thermal conduction (McDonald et al. 2010), and reconnection diffusion (Fabian et al. 2011). However, individually, none of the ionization mechanisms listed can account for all line ratios simultaneously. As shown in Figure 4, line ratios measured in 3CR 318.1 show extremely low values of $[\text{O III}]/\text{H}\beta$ in the diagnostic diagrams; similarly, McDonald et al. (2012) found systematically lower $[\text{O III}]/\text{H}\beta$ values in filaments of cool core galaxy clusters and higher values of $[\text{N II}]/\text{H}\alpha$, $[\text{O I}]/\text{H}\alpha$, and $[\text{S II}]/\text{H}\alpha$ than those found in galaxies in the SDSS. Although the diagnostic diagrams are used to discriminate between star-forming and AGN-dominated galaxies, they tend to fail when the ionization is due to more complex situations and/or different ionization mechanisms (see, e.g., Stasińska et al. 2008; Capetti & Baldi 2011; Balmaverde et al. 2018) and therefore they may have a limited validity in assessing the ionization conditions of BCGs. Thus, the line ratios in 3CR 318.1 imply that the emission from the filaments is due to a combination of ionization mechanisms. McDonald et al. (2012) suggested that line ratios are due to a combination of star formation and ionization from slow shocks (~ 100 – 400 km s $^{-1}$; see also Allen et al. 2008). Since our results are similar to those of McDonald et al. (2012), we argue that their conclusion applies also to the case of 3CR 318.1. An additional contribution from self-ionizing cooling ICM is suggested by the low velocity dispersion (~ 60 km s $^{-1}$) of the optical filaments in 3CR 318.1, which implies a small contribution of shocks to the total ionization. Therefore, we conclude that the underlying ionization mechanisms include a combination of photoionization due to star formation, self-

ionizing cooling ICM, and a small contribution of ionization due to slow shocks. Additionally, although McDonald et al. (2012) already found a decrease of the emission line width with radius, thanks to the MUSE data, it was discovered that this decrease occurs sharply in the case of 3CR 318.1 (from ~ 200 km s $^{-1}$ in the core to ~ 60 km s $^{-1}$ along the filaments; see Balmaverde et al. 2019).

We detected an excess of X-ray emission above the ICM along the $[\text{N II}]\lambda 6584$ filaments. This X-ray filament is colder and despite the large uncertainties, appears to have a lower metal abundance than the surrounding ICM, in agreement with literature results (McDonald et al. 2010). The association between the X-ray and optical filamentary morphologies, together with the radio structure, suggests that the filaments could have originated from AGN-driven outflows in the direction of the radio jet. This scenario is in agreement with the smooth 0.5–3 keV X-ray surface brightness profile at the location of the $[\text{N II}]\lambda 6584$ filament and with simulations carried out by Qiu et al. (2019, 2020), in which cold filaments originate from warm outflows (10^4 – 10^7 K). Additionally, works such as Gaspari et al. (2018) and Voit (2021) predict that optical emission line nebulae would present velocity dispersions of ~ 100 – 200 km s $^{-1}$ in the cases where the nebulae originated from compression and catastrophic cooling (see also Gaspari et al. 2012, 2013, 2015, 2017; Voit et al. 2017 for previous works on multiphase condensation). However, the $[\text{N II}]\lambda 6584$ filaments in 3CR 318.1 present very low velocity dispersions (~ 60 km s $^{-1}$; see Figure 8 in Balmaverde et al. 2019), so the AGN uplift scenario could be favored.

We thank the anonymous referee for their useful comments that led to the improvement of the paper. This work is supported by the “Departments of Excellence 2018–2022 Grant” awarded by the Italian Ministry of Education, University and Research (MIUR) (L. 232/2016). This research has made use of resources provided by the Ministry of Education, Universities and Research for the grant MASF_F-FABR_17_01. This investigation is supported by the National Aeronautics and Space Administration (NASA) grants GO9-20083X and GO0-21110X. F.M. is indebted to S. Bianchi for his valuable input on X-ray photoionization scenarios. A.J. acknowledges the financial support (MASF_CONTR_FIN_18_01) from the Italian National Institute of Astrophysics under the agreement with the Instituto de Astrofísica de Canarias for the “Becas Internacionales para Licenciados y/o Graduados Convocatoria de 2017.” A.P. acknowledges financial support from the Consorzio Interuniversitario per la fisica Spaziale (CIFS) under the agreement related to the grant MASF_CONTR_FIN_18_02. W.F. and R.K. acknowledge support from the Smithsonian Institution and the Chandra High Resolution Camera Project through NASA contract NAS8-03060. G.V. acknowledges support from ANID programs FONDECYT Postdoctorado 3200802 and Basal-CATA AFB-170002.

ORCID iDs

- A. Jimenez-Gallardo <https://orcid.org/0000-0003-4413-7722>
- F. Massaro <https://orcid.org/0000-0002-1704-9850>
- B. Balmaverde <https://orcid.org/0000-0002-0690-0638>
- A. Paggi <https://orcid.org/0000-0002-5646-2410>
- A. Capetti <https://orcid.org/0000-0003-3684-4275>

- W. R. Forman [ID](https://orcid.org/0000-0002-9478-1682) <https://orcid.org/0000-0002-9478-1682>
 R. P. Kraft [ID](https://orcid.org/0000-0002-0765-0511) <https://orcid.org/0000-0002-0765-0511>
 R. D. Baldi [ID](https://orcid.org/0000-0002-1824-0411) <https://orcid.org/0000-0002-1824-0411>
 V. H. Mahatma [ID](https://orcid.org/0000-0001-5221-2636) <https://orcid.org/0000-0001-5221-2636>
 C. Mazzucchelli [ID](https://orcid.org/0000-0002-5941-5214) <https://orcid.org/0000-0002-5941-5214>
 V. Missaglia [ID](https://orcid.org/0000-0001-8382-3229) <https://orcid.org/0000-0001-8382-3229>
 F. Ricci [ID](https://orcid.org/0000-0001-5742-5980) <https://orcid.org/0000-0001-5742-5980>
 G. Venturi [ID](https://orcid.org/0000-0001-8349-3055) <https://orcid.org/0000-0001-8349-3055>
 E. Liuzzo [ID](https://orcid.org/0000-0003-0995-5201) <https://orcid.org/0000-0003-0995-5201>
 C. P. O'Dea [ID](https://orcid.org/0000-0001-6421-054X) <https://orcid.org/0000-0001-6421-054X>
 M. A. Prieto [ID](https://orcid.org/0000-0002-3585-2639) <https://orcid.org/0000-0002-3585-2639>
 H. J. A. Röttgering [ID](https://orcid.org/0000-0001-8887-2257) <https://orcid.org/0000-0001-8887-2257>
 E. Sani [ID](https://orcid.org/0000-0002-3140-4070) <https://orcid.org/0000-0002-3140-4070>
 W. B. Sparks [ID](https://orcid.org/0000-0002-9011-6829) <https://orcid.org/0000-0002-9011-6829>
 G. R. Tremblay [ID](https://orcid.org/0000-0002-5445-5401) <https://orcid.org/0000-0002-5445-5401>
 R. J. van Weeren [ID](https://orcid.org/0000-0002-0587-1660) <https://orcid.org/0000-0002-0587-1660>
 B. J. Wilkes [ID](https://orcid.org/0000-0003-1809-2364) <https://orcid.org/0000-0003-1809-2364>
 J. J. Harwood [ID](https://orcid.org/0000-0003-0251-6126) <https://orcid.org/0000-0003-0251-6126>
 P. Mazzotta [ID](https://orcid.org/0000-0002-5411-1748) <https://orcid.org/0000-0002-5411-1748>
 J. Kuraszkiewicz [ID](https://orcid.org/0000-0001-5513-029X) <https://orcid.org/0000-0001-5513-029X>

References

- Allen, M. G., Groves, B. A., Dopita, M. A., et al. 2008, *ApJS*, 178, 20
 Bacon, R., Accardo, M., Adjali, L., et al. 2010, *Proc. SPIE*, 7735, 773508
 Baldwin, J. A., Phillips, M. M., & Terlevich, R. 1981, *PASP*, 93, 5
 Balmaverde, B., Capetti, A., Grandi, P., et al. 2012, *A&A*, 545, A143
 Balmaverde, B., Capetti, A., Marconi, A., et al. 2018, *A&A*, 612, A19
 Balmaverde, B., Capetti, A., Marconi, A., et al. 2019, *A&A*, 632, A124
 Bennett, A. S. 1962, *MNRAS*, 125, 75
 Bennett, C. L., Larson, D., Weiland, J. L., & Hinshaw, G. 2014, *ApJ*, 794, 135
 Bîrzan, L., Rafferty, D. A., Brüggen, M., et al. 2020, *MNRAS*, 496, 2613
 Capetti, A., & Baldi, R. D. 2011, *A&A*, 529, A126
 Capetti, A., Brienza, M., Baldi, R. D., et al. 2020, *A&A*, 642, A107
 Capetti, A., Robinson, A., Baldi, R. D., et al. 2013, *A&A*, 551, A55
 Cardelli, J. A., Clayton, G. C., & Mathis, J. S. 1989, *ApJ*, 345, 245
 Conselice, C. J., Gallagher, J. S., III, & Wyse, R. F. G. 2001, *AJ*, 122, 2281
 Dopita, M. A., & Sutherland, R. S. 1995, *ApJ*, 455, 468
 Edge, D. O., Shakeshaft, J. R., McAdam, W. B., et al. 1959, *MmRAS*, 69, 37
 Edwards, L. O. V., Robert, C., Mollá, M., et al. 2009, *MNRAS*, 396, 1953
 Fabian, A. C., Johnstone, R. M., Sanders, J. S., et al. 2008, *Natur*, 454, 968
 Fabian, A. C., Sanders, J. S., Williams, R. J. R., et al. 2011, *MNRAS*, 417, 172
 Freeman, P., Doe, S., & Siemiginowska, A. 2001, *Proc. SPIE*, 4477, 76
 Fruscione, A., McDowell, J. C., Allen, G. E., et al. 2006, *Proc. SPIE*, 6270, 62701V
 Gaspari, M., Brightenti, F., & Temi, P. 2015, *A&A*, 579, A62
 Gaspari, M., McDonald, M., Hamer, S. L., et al. 2018, *ApJ*, 854, 167
 Gaspari, M., Ruszkowski, M., & Oh, S. Peng 2013, *MNRAS*, 432, 3401
 Gaspari, M., Ruszkowski, M., & Sharma, P. 2012, *ApJ*, 746, 94
 Gaspari, M., Temi, P., & Brightenti, F. 2017, *MNRAS*, 466, 677
 Giacintucci, S., Venturi, T., Murgia, M., et al. 2007, *A&A*, 476, 99
 Jimenez-Gallardo, A., Massaro, F., Paggi, A., et al. 2021, *ApJS*, 252, 31
 Jimenez-Gallardo, A., Massaro, F., Prieto, M. A., et al. 2020, *ApJS*, 250, 7
 Kalberla, P. M. W., Burton, W. B., Hartmann, D., et al. 2005, *A&A*, 440, 775
 Kauffmann, G., Heckman, T. M., Tremonti, C., et al. 2003, *MNRAS*, 346, 1055
 Kewley, L. J., Groves, B., Kauffmann, G., et al. 2006, *MNRAS*, 372, 961
 Kewley, L. J., Heisler, C. A., Dopita, M. A., et al. 2001, *ApJS*, 132, 37
 Laing, R. A., Riley, J. M., & Longair, M. S. 1983, *MNRAS*, 204, 151
 Lynds, R. 1970, *ApJL*, 159, L151
 Massaro, F., Álvarez-Crespo, N., Capetti, A., et al. 2019, *ApJS*, 240, 20
 Massaro, F., Capetti, A., Paggi, A., et al. 2020, *ApJS*, 247, 71
 Massaro, F., Capetti, A., Paggi, A., et al. 2020, *ApJL*, 900, L34
 Massaro, F., Giommi, P., Tosti, G., et al. 2008b, *A&A*, 489, 1047
 Massaro, F., Harris, D. E., & Cheung, C. C. 2011a, *ApJS*, 197, 24
 Massaro, F., Harris, D. E., Liuzzo, E., et al. 2015, *ApJS*, 220, 5
 Massaro, F., Harris, D. E., Tremblay, G. R., et al. 2013, *ApJS*, 206, 7
 Massaro, F., Missaglia, V., Stuardi, C., et al. 2018, *ApJS*, 234, 7
 Massaro, F., Tramacere, A., Cavaliere, A., et al. 2008a, *A&A*, 478, 395
 Mazzotta, P., Brunetti, G., Giacintucci, S., et al. 2004, *JKAS*, 37, 381
 Mazzotta, P., Kaastra, J. S., Paerels, F. B., et al. 2002, *ApJL*, 567, L37
 McDonald, M., Veilleux, S., Rupke, D. S. N., et al. 2010, *ApJ*, 721, 1262
 McDonald, M., Veilleux, S., & Rupke, D. S. N. 2012, *ApJ*, 746, 153
 Morgan, W. W., Kayser, S., & White, R. A. 1975, *ApJ*, 199, 545
 Osterbrock, D. E. 1989, *Astrophysics of Gaseous Nebulae and Active Galactic Nuclei* (Mill Valley, CA: Univ. Science Books)
 Peres, C. B., Fabian, A. C., Edge, A. C., et al. 1998, *MNRAS*, 298, 416
 Qiu, Y., Bogdanović, T., Li, Y., et al. 2019, *ApJL*, 872, L11
 Qiu, Y., Bogdanović, T., Li, Y., et al. 2020, *NatAs*, 4, 900
 Sabater, J., Best, P. N., & Argudo-Fernández, M. 2013, *MNRAS*, 430, 638
 Sanders, J. S., & Fabian, A. C. 2007, *MNRAS*, 381, 1381
 Spinrad, H., Djorgovski, S., Marr, J., & Aguilar, L. 1985, *PASP*, 97, 932
 Stasińska, G., Vale Asari, N., Cid Fernandes, R., et al. 2008, *MNRAS Letters*, 391, L29
 Voit, G. M. 2021, *ApJL*, 908, L16
 Voit, G. M., Donahue, M., & Slavin, J. D. 1994, *ApJS*, 95, 87
 Voit, G. M., Meece, G., Li, Y., et al. 2017, *ApJ*, 845, 80
 Worpel, H., Brown, M. J. I., Jones, D. H., et al. 2013, *ApJ*, 772, 64